Targeted Modulation of Photocatalytic Hydrogen Evolution Activity by Nickel-Substituted Rubredoxin through Functionalized Ruthenium Phototriggers

Ashlee E. Wertz[†], Sean C. Marguet[†], Claudia Turro[†], Hannah S. Shafaat^{†,&*}

[†]Department of Chemistry and Biochemistry, The Ohio State University; 100 W 18th Ave, Columbus, OH 43210

[&]Department of Chemistry and Biochemistry, University of California, Los Angeles; 607 Charles E. Young Drive East, Los Angeles, CA 90095

ABSTRACT Light-driven hydrogen evolution is a promising means of sustainable energy production to meet the global energy demand. This study investigates the photocatalytic hydrogen evolution activity of nickel-substituted rubredoxin (NiRd), an artificial hydrogenase mimic, covalently attached to a ruthenium phototrigger (RuNiRd). By systematically modifying the *para*-substituents on Ru(II) polypyridyl complexes, we sought to optimize the intramolecular electron transfer (ET) processes within the RuNiRd system. A series of

electron-donating and electron-withdrawing groups were introduced to tune the photophysical, photochemical, and electrochemical properties of the ruthenium complexes. Our findings reveal that electron-donating substituents can increase the hydrogen evolution capabilities of the artificial enzyme to a point; however, the complexes with the most electron donating substituents suffer from short lifetimes and inefficient reductive quenching, rendering them inactive. The present work highlights the intricate balance required between driving force, lifetime, and quenching efficiency for effective light-driven catalysis, providing valuable insights for the design of artificial enzyme-photosensitizer constructs.

INTRODUCTION

The worldwide energy demand is rapidly rising due to population and industrial growth.¹ Addressing the growing energy needs while mitigating the environmental impact requires a shift towards renewable energy sources. Sunlight has emerged as a promising source of green energy, offering an environmentally sustainable alternative to conventional fossil fuels.²⁻⁵ Solar fuels, such as hydrogen, serve as energy carriers with storage capabilities and high-density energy outputs.⁶⁻¹⁰ Photocatalysis can play a pivotal role in harnessing solar radiation.¹¹⁻¹⁵ One strategy in photocatalyst development involves the covalent attachment of a photosensitizer to a native or artificial enzyme. These covalently tethered constructs circumvent the need for diffusive collisional contact, allowing for rapid and efficient charge separation (**Figure 1A**).¹⁶ Furthermore, covalently attaching a photosensitizer to an enzyme has provided insight into catalytic processes and intermediates.¹⁷⁻¹⁹ There are many strategies for covalent attachment

using the reactivity of amino acid residues such as lysine, histidine, and cysteine.^{20–23} Among them, cysteine is a convenient target for modification due to lower natural protein abundance and the strongly nucleophilic sulfhydryl side chain.²⁴

Several types of photosensitizers, including inorganic compounds, organic dye molecules, and nanomaterials, have successfully been conjugated to enzymes to overcome a high photocatalytic overpotential.^{25,26} Ru(II) polypyridyl complexes are a popular choice due to their long-lived excited states, redox properties, and light absorption in the visible range.^{27–32} Previously, we have developed a photocatalytic system for light-driven hydrogen evolution based on nickel-substituted rubredoxin coupled to a Ru(II) complex (Ru(bpy)NiRd) as an artificial hydrogenase mimic,^{33–35} where the chromophore [Ru^{II}(bpy)₂(epoxy-phen)]²⁺) (bpy = 2,2'-bipyridine; epoxy-phen = 5,6-epoxy-5,6-dihydro-[1,10]phenanthroline) was covalently bound to a surface-exposed cysteine residue adjacent to the active site (**Figure 1B**). It was shown that covalently attaching the Ru chromophore to NiRd in Ru(bpy)NiRd resulted in an 8-fold increase in activity for light-driven hydrogen evolution compared to stoichiometric

amounts of $[Ru(bpy)_3]^{2+}$ and NiRd in solution,³⁶ and time-resolved spectroscopy revealed direct intramolecular electron transfer (ET) between the metal centers.^{36,37}

However, because of the relative free energies for oxidative quenching relative to reductive quenching, the intramolecular ET process was attributed to the formation of a catalytically unproductive [Ru]+Ni³+ state. Here, to optimize the photocatalytic activity of the Ru(L)NiRd system, we have generated a series of ruthenium complexes where the bpy ligands are substituted in the 4,4'-position (*para* to the coordinating N atoms), Ru(L)NiRd, to systematically tune the photophysical and excited state reduction potentials of the chromophore (**Figure 1C**). We hypothesized that more favorable ET to the Ni center may

light-driven increase H_2 evolution through direct photoinduced formation of the catalytically relevant [Ru]3+Ni+ intermediate.35 The investigated substituents include electron-withdrawing -COOH (dcbpy) and -CF₃ (btfmb), as well as electrondonating $-N(CH_3)_2$ (dmabpy), -OCH₃ (meob), –CH₃ (dmb), and

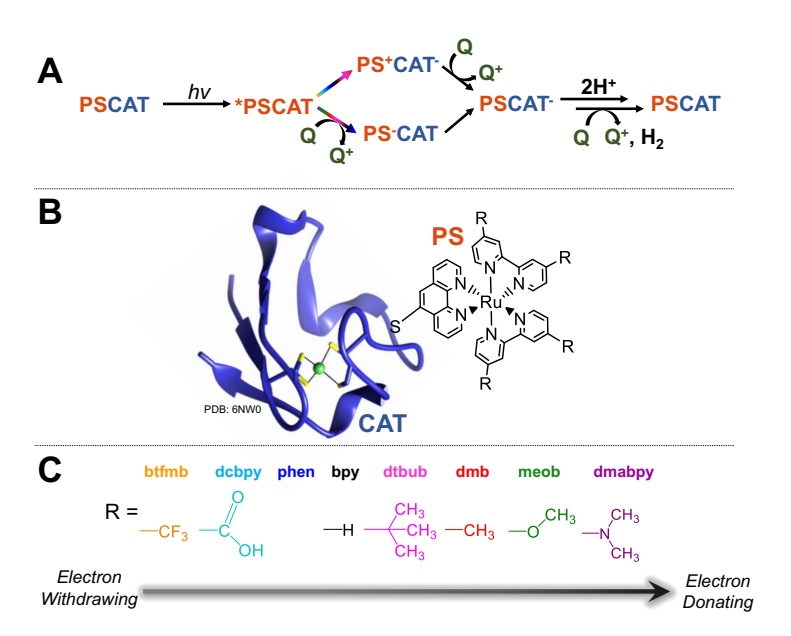


Figure 1. (**A**) Schematic of possible mechanisms for photoinduced hydrogen production by a tethered photosensitizer (**PS**)-catalyst (**CAT**) construct in the presence of a reductive quencher (**Q**). (**B**) Cartoon showing RuNiRd **PSCAT** system developed in this work with parasubstituted ruthenium phototriggers. (**C**) Schematic

 $-C(CH_3)_3(dtbub))$ groups at the *para* positions of the ancillary bipyridine ligands. The influence

of using 1,10-phenantholine (phen) instead of bpy was also investigated. As predicted, varying the driving force to favor the putative catalytically relevant intermediate increased hydrogen production. However, interestingly, the complexes with the most electron donating substituents, Ru(dmabpy)NiRd and Ru(meob)NiRd, were completely inactive for hydrogen evolution. Using a suite of photophysical techniques for characterization, this inactivity was attributed to a combination of short excited state lifetimes and low intermolecular quenching rates, highlighting the complex interplay involved in fine-tuning artificial enzyme-photosensitizer constructs.

MATERIALS AND METHODS

Materials

The following ligands were purchased from the specified supplier: 2,2'-bipyridine (bpy, Alfa Aesar), 4,4'-dimethyl-2,2'- bipyridine (dmb, Alfa Aesar), 1,10-phenanthroline (phen, Sigma Aldrich), 4,4'-dimethoxy-2,2'-bipyridine (meob, Sigma Aldrich), 4,4'-di-tert-butyl-2,2'-dipyridyl (dtbub, Sigma Aldrich), 4,4'-bis(trifluoromethyl-2,2'-bipyridine) (btfmb, Strem Chemical), 2,2'-bipyridine-4,4'-dicarboxylic acid (dcbpy, Beantown Chemical) and 4,4'-bis(N,N-dimethylamino)-2,2'-bipyridine (dmabpy, BLD Pharmatech).

Protein expression and purification

The *Desulfovibrio desulfuricans* rubredoxin (Rd) was heterologously expressed, purified, and metalated as previously described.^{34,35} ZnRd was prepared by metal substitution with ZnSO₄ using purified FeRd protein.

Synthesis of $[Ru(L)_3][(PF_3)_2]$, (L = bpy, meob, dmb, dmabpy, and phen)

The following preparation of these compounds was modified from Broomhead et al (Figure S1A).38 RuCl3•H2O (0.083 g, 0.40 mmol) was added to 8 mL of deionized water and stirred until RuCl₃ was fully dissolved. While stirring, 1.2 mmol of ligand (bpy, 0.188 g; dmb, 0.222 g; phen, 0.217 g; meob, 0.260g and dmabpy, 0.291 g) and 500 μL of 6 M aqueous NaH₂PO₂ were added to the solution. The reaction mixture was refluxed for 30 minutes until the solution turned a deep orange color. The solution was allowed to cool to room temperature, then placed in a -20 °C freezer for 5 minutes. Approximately 1-2 mL of a saturated ammonium hexafluorophosphate (NH₄PF₆, Thermo Fisher) solution was added to precipitate out an orange solid, which was collected via vacuum filtration. The solid was washed with two 1-mL portions of chilled water and 5 mL of diethyl ether. The solid was dried with vacuum filtration for 20 minutes, then dissolved in acetonitrile. The solution was centrifuged at 17,000xg for 10 minutes, then the supernatant was precipitated by addition into 5 mL of cooled diethyl ether. The solid was filtered via vacuum filtration for 20 minutes and allowed to dry overnight. Yields ranged from 24-75 %.

Synthesis of $[Ru(L)_3][(PF_3)_2]$, (L = dtbub, dcbpy, and btfmb)

The following preparation of these compounds was modified from Rillema et al (Figure S1B).³⁹ RuCl₃·H₂O (0.083 g, 0.40 mmol) was added in 10 mL of ethylene glycol and stirred until RuCl₃ was dissolved. While stirring, 1.2 mmol of ligand (dtbub, 0.322 g; btfmb, 0.351 g; and dcbpy, 0.293 g) was added into the solution. The reaction mixture was refluxed 1-3 hours until solution turned a deep orange or dark red color. Solution was allowed to cool to room

temperature then placed in -20 °C freezer for 5 minutes. Approximately 1-2 mL of a saturated NH₄PF₆ solution was added to precipitate out an orange or brown solid and collected via vacuum filtration. Solid was washed with two 1 mL portions of chilled water and 5 mL of diethyl ether. The solid was dried with vacuum filtration for 20 minutes, then dissolved in acetonitrile. Solution was centrifuged at 17,000xg for 10 minutes, then supernatant was precipitated by addition into 5 mL of cooled diethyl ether. Solid was filtered via vacuum filtration for 20 minutes and allowed to dry overnight. Yields ranged from 50-75 % based on the starting ruthenium amount.

Synthesis of cis-Ru(L)₂Cl₂·H₂O (L = dmabpy, meob, dmb, bpy, phen, dcbpy and btfmb)

Cis-Ru(L)₂Cl₂·H₂O was synthesized according to the following procedure modified from Coudret et al (Figure S1C).^{40,41} RuCl₃·3H₂O (0.25 g, 1 mmol) was added to a solution of LiCl (1.7 g, 39 mmol) in ethylene glycol/water (25 mL, 4:1) at 110° C. After 15 min, 2 mmol of ligand (dmabpy, 0.54 g; meob, 0.43 g; 0.37 g, dmb; 0.31 g, bpy; 0.36 g, phen; 0.49 g, dcbpy; 0.58 g, btfmb) was added. After 12 min, glucose (0.36 g, 2.0 mmol) was added and allowed to react for 10 min, at which point ascorbic acid (0.089 g, 0.5 mmol) was added. The reaction solution was maintained at 110° C for 30 min. The reaction was quenched with the addition of 10 mL of a saturated NaCl solution and cooled to 0° C for 60 min. The purple precipitate was filtered and washed with the NaCl solution. Yields ranged from 50-75%.

Synthesis of cis-Ru(L)₂Cl₂·H₂O (L = dtbub)

Cis-[Ru(4,4'-Di-tert-butyl-2,2'-bipyridine)₂Cl₂ RuCl₃·3H₂O (0.25 g, 1 mmol) was added to a solution of LiCl (1.7 g, 39 mmol) in ethylene glycol/water (24 mL, 5:1) at 110 °C. After 15 min,

2 mmol of ligand (dtbub, 0.43 g) was added. Glucose was added after 25 minutes (0.36 g, 2.0 mmol, 2 eq) and allowed to react for 10 min. Increased ascorbic acid was used (0.12 g, 0.7 mmol, 0.7 eq) and once added, the reaction solution was maintained at 110° C for 30 min. The reaction was quenched with the addition of 10 mL of a saturated NaCl solution and cooled to 0°C for 60 min. The dark purple precipitate was filtered and washed with the NaCl solution. The viscous violet solution yielded a dark violet precipitate after vacuum filtration. The resultant powder was dissolved in ethyl acetate, and the insoluble component was filtered off. The product was recrystallized with the dropwise addition of hexane to yield a fine black powder (64% yield).

Synthesis of $[Ru(L)_2(epoxy-phen)][(PF_6)_2]$

The following preparation of these Ru-phototriggers was adapted from Dwaraknath et al (Figure S1D).²¹ 0.09 mmol cis-Ru(L)₂Cl₂ (dmabpy, 0.059; bpy, 0.043 g; dmb, 0.049 g; phen, 0.048 g; meob, 0.054 g; dtbub, 0.064 g; btfmb, 0.068 g; and dcbpy, 0.059 g) was dissolved in 5 mL of a 75:25 ethanol:water mixture. The mixture was stirred until solid was dissolved. 0.018 g of 5,6-epoxy-5,6-dihydro[1,10]phenanthroline (epoxy-phen, 0.09 nmol; Sigma Aldrich) was added into the solution. Solution was placed under foil to avoid light exposure and refluxed for 3 hours at 100 °C while stirring. After reflux, solution was allowed to cool to room temperature, and the ethanol was evaporated via a stream of N₂ gas. Solution was chilled in the -20 °C freezer for 5 mins, and approximately 1-2 mL of a saturated NH₄PF₆ solution was added to precipitate an orange or brown solid. The precipitate was filtered via vacuum filtration and washed with 1 mL of chilled water and 5 mL of diethyl ether. The solid was dried

with vacuum filtration for 20 minutes, then dissolved in acetonitrile. Solution was centrifuged at 17,000xg for 10 minutes, then supernatant was precipitated by addition into 5 mL of cooled diethyl ether. Solid was filtered via vacuum filtration for 20 minutes and allowed to dry overnight. Yields ranged from 90- 95% based on the starting ruthenium amount. Synthesis was confirmed via MALDI-TOF spectrometry (Figure S2).

Covalent attachment of [Ru(L)2(epoxy-phen)][(PF6)2] to rubredoxin (Ru(L)MRd)

ZnRd, FeRd, or NiRd (MRd) were used for protein labeling reactions. Protein was reduced by the addition of dithiothreitol (DTT) to a final concentration of $2.4\ x$ MRd. The MRd + DTT solution was incubated at room temperature for 5-10 minutes to ensure reduction of the C31 thiol. It was observed that incubation durations of greater than 10 minutes could result in chelation of the metal ion by DTT. Excess DTT was removed via Econo-Pac 10-DG Desalting column and the MRd was collected. For ZnRd, the fractions were assessed by Bradford reagent due to ZnRd lacking visible electronic absorption. The labeling reactions were then prepared by dilution of MRd to a final concentration of 25 μM with 100 μM Ru-phototrigger in 50% (v/v) of 50 mM Tris, pH 8.0 and 50 % (v/v) of 50 mM CHES, pH 9.0. Reaction mixtures were stirred at room temperature for 48 hours. After incubation, the labeling reactions were concentrated by 3 kDa NMWCO Amicon stirred cell membrane (Millipore Sigma, St. Louis, MO) and centricons to approximately 500 μL. Excess Ru-phototrigger was removed using an Econo-Pac 10-DG Desalting column equilibrated with 50 mM Tris, pH 8.0. If excess Ruphototrigger was present, the labeled protein was pooled and incubated with 10% v/v acetonitrile overnight at 4°C. A HiTrap-Q anion exchange column was used to remove

unlabeled protein from the reaction mixture (Figure S3). The concentration of NiRd or FeRd was determined for the Ru(L)NiRd and Ru(L)FeRd samples using the extinction coefficients for the d-d charge transfer transitions (NiRd ϵ_{740} = 390 M⁻¹cm⁻¹, FeRd ϵ_{755} = 530 M⁻¹cm⁻¹). The concentration of the Ru phototrigger was determined using the extinction coefficient at 451 nm (Table S1) and subtracting any absorbance present from Rd (NiRd ϵ_{451} = 3310 M⁻¹cm⁻¹, FeRd ϵ_{451} = 5150 M⁻¹cm⁻¹). For the Ru(L)ZnRd samples, the concentration of the Ru phototrigger was determined through the extinction coefficient at 451 nm and the concentration of ZnRd was determined at 286 nm (ZnRd ϵ_{286} =10200 M⁻¹cm⁻¹), subtracting any absorbance due to the Ru phototrigger (Table S1).

UV-Visible spectroscopy

All UV-visible absorbance measurements were collected with a quartz cuvette using an Agilent 8453 diode array spectrometer.

MALDI-TOF mass spectrometry

MALDI-TOF samples were prepared on a ground steel plate (Bruker MSP 96 microScout Target) using a matrix made of 100 mM sinapinic acid (Sigma) in 60/30/10 v/v/v water/acetonitrile/0.1% trifluoroacetic acid. For all samples, 1 μ L of sample/matrix was deposited onto the plate and allowed to dry completely before analysis. All measurements were carried out with a Bruker microFlex MALDI-TOF mass spectrometer operating in positive-ion mode.

Electrochemistry

All electrochemistry experiments were performed in acetonitrile with a [Ru(L)₃]²⁺ concentration of 1 mM and 100 mM tetra-N-butylammonium hexafluorophosphate (TBAPF₆, Acros Organics or Sigma-Aldrich) as a supporting electrolyte under a headspace of N₂ gas. A three-electrode system was used with a glassy carbon working electrode, a Pt-wire counter electrode, and a Ag/AgCl reference electrode. A small amount of ferrocene was added as a reference. Cyclic voltammograms were measured with a WaveNow potentiostat (Pine Research Instrumentation) or an EC Epsilon EClipse potentiostat with a scan rate of 50 mV/s. Reduction potentials were measured versus Fc+/Fc couple, but converted to NHE by the addition of +0.63 V.⁴²

Gas chromatography assays

All samples were prepared under an anaerobic N₂ atmosphere (ErlabTM Portable Pyramid Enclosure Glove Bag). Gas chromatograph (GC) samples were prepared in a 20 mL septum-sealed glass vial with a total solution volume of 3 mL. Hydrogen production was measured on a Shimazu GC-2014 equipped with TCD detection. Assays were conducted in a custom-built glass cell and chilled to 4°C. Samples were illuminated by four evenly spaced LUXEON Rebel ES LEDs placed below the cell (447 nm, ~ 2 cm from sample) and strands of blue LEDs (Home EVER Inc., Las Vegas, NV) around the cell (450 nm, ~3 cm from sample). The average irradiation power was approximately 20 mW. Ru(L)NiRd samples were composed of 10 μM Ru(L)NiRd + 100 mM ascorbate while unlabeled protein samples consisted of 10 μM [Ru(L)₃]²⁺ + 10 μM NiRd + 100 mM ascorbate. All samples were in 1 M phosphate buffer, pH 6.5. Reported values were corrected for the samples to have the same absorbance at 451 nm.

Luminescence and time-correlated single-photon counting experiments

All room temperature samples were prepared under an anaerobic N₂ atmosphere (ErlabTM Portable Pyramid Enclosure Glove Bag) and further sparged with N2 gas to prevent quenching from oxygen.⁴³ All samples were diluted into 1 M phosphate, pH 6.5, in 0.2 x 1 cm gastight quartz cuvettes (FireflySci) such that the absorbance at around 450 nm was between 0.05 and $0.1 (0.05 < A_{451} < 0.1;$ approximately 5-10 μ M Ru). Room temperature emission spectra were recorded on a Horiba Scientific Fluorolog-3 spectrofluorometer with excitation at 455 nm, and emission was monitored from 500 to 800 nm with an integration time of 1 sec and bandpass of 5 nm. Time-resolved single photon counting (TCSPC) emission measurements were carried out with the same samples as those for emission spectral measurements using a NanoLED-455 diode with pulse width for 1.3 ns and excitation wavelength of 451 nm, coupled to a Horiba Scientific Fluorolog-3 spectrofluorometer for monitoring at the emission maximum with an appropriate bandpass (4-14 nm) to give a stop rate of less than 2%. The lifetimes of the complexes with the electron donating substituents were sufficiently short to need to consider the instrument response function. Therefore, a measurement of water was taken and overlaid on the kinetic traces of each complex to determine the relevant region for fitting. When fitting the Ru(L)NiRd and Ru(L)FeRd complexes, τ₂ and τ₃ were fixed at the values determined for Ru(L)ZnRd. E₀₀ values for [Ru(L)₃][(PF₃)₂] samples were obtained at 77 K on a Horiba FluoroMax-4 Spectrofluorometer using a 515 nm longpass filter with excitation at 455 nm and emission monitored from 515 to 800 nm (Figure S4).

Stern-Volmer analysis was performed on the $[Ru(L)_3]^{2+}$ series using both luminescence and TCPSC measurements with varying amounts of ascorbate added to the sample. The dynamic portion of the observed quenching was determined through lifetime measurements using Eq. 1

$$\frac{\tau_0}{\tau} = 1 + K_D[Q] \tag{1}$$

where τ is the lifetime in the presence of quencher (Q), τ_0 is the lifetime in the absence of quencher, and $K_D = k_q \tau_0$.⁴⁴ The static quenching constant was determined through fitting emission intensity measurements using Eq. 2

$$\frac{I_0}{I} = (1 + K_D[Q])(1 + K_S[Q]) \tag{2}$$

where I is the emission intensity in the presence of quencher, I₀ is the intensity in the absence of quencher and K_S is the association constant for complex formation. K_D was held at the value obtained from fitting the lifetime measurements. The relative contributions of dynamic and static quenching were resolved by considering the ratio of K_D/K_S as given in Table 1.

Excited State Reduction Potential Determination

The excited state reduction potentials of the $[Ru(L)_3]^{2+}$ series were calculated using Eqs. 3 and 4^{45}

$$E(Ru^{3+/2+*}) = E(Ru^{3+/2+}) - E_{00}(Ru^{2+*/2+})$$
(3)

$$E(Ru^{2+^*/+}) = E(Ru^{2+/+}) + E_{00}(Ru^{2+^*/2+})$$
(4)

where $E_{00}(Ru^{2+^{*}/2+})$ is the potential equivalent to the electronic energy of the excited state determined through 77 K emission experiments.

Photoluminescence (PL) quantum yield measurements

Quantum yields were calculated using Eq. 5

$$\Phi = \Phi_{ref}(\frac{A_{ref}}{A})(\frac{I}{I_{ref}}) \tag{5}$$

where Φ_{ref} is the quantum yield of the reference complex $[Ru(bpy)_3]^{2+}$ ($\Phi=0.042$). Aref is the absorbance of $[Ru(bpy)_3]^{2+}$ at the excitation wavelength ($\lambda_{ex}=455$ nm), A is the absorbance of the sample at the excitation wavelength, I is the integrated area under the emission spectrum of the sample, and I_{ref} is the integrated area under the emission spectrum of the $[Ru(bpy)_3]^{2+}$.

Nanosecond transient absorption experiments

All samples were prepared under an anaerobic N_2 atmosphere (ErlabTM Portable Pyramid Enclosure Glove Bag). Samples contained ~50 µM RuMRd in 1 M phosphate buffer at pH 6.5 in a 0.2 x 1 cm gastight quartz cuvette. All nanosecond transient absorption (TA) single-wavelength data were collected using a pump pulse from the second harmonic frequency of a Nd:YAG laser (532 nm) operating at 10 Hz (Spectra Physics, Quanta-Ray) and a CW Xe probe light coupled with a monochromator and photomultiplier tube (Products for Research, Inc). All samples were pumped with 40 ± 2 mW of power.

RESULTS

Electronic absorption spectra of $[Ru(L)_3]^{2+}$ and $[Ru(L)_2(epoxy-phen)]^{2+}$ complexes

The electronic absorption spectra of the $[Ru(L)_3]^{2+}$ and $[Ru(L)_2(epoxy-phen)]^{2+}$ series measured in 1 M PO₄ buffer at pH 6.5 exhibit a typical ligand-centered (LC) $\pi \to \pi^*$ transition in the UV and metal-to-ligand charge transfer (MLCT) $d\to\pi^*$ transitions in the visible spectral region (Figure S5).⁴⁷ Across both series, the $\pi\to\pi^*$ transition primarily shifts to lower energies as the substituent becomes more electron withdrawing (**Table 1**, Table S2). A general shift to lower energies is observed for the MLCT transition across both $[Ru(L)_3]^{2+}$ and $[Ru(L)_2(epoxy-phen)]^{2+}$ series as the bpy substituent becomes more electron donating or electron withdrawing, with those of $[Ru(dmabpy)_3]^{2+}$ and $[Ru(dmabpy)_2(epoxy-phen)]^{2+}$ observed at significantly longer wavelengths than the unsubstituted compounds (**Table 1**, Table S2).

Photophysical properties of [Ru(L)₃]²⁺ and [Ru(L)₂(epoxy-phen)]²⁺ complexes

Time resolved and steady state luminescence experiments were performed on the $[Ru(L)_3]^{2+}$ and $[Ru(L)_2(epoxy-phen)]^{2+}$ series to evaluate the photophysical properties in aqueous solution under catalytically relevant conditions. Upon excitation into the MLCT band of each Ru

Table 1. MLCT and $\pi\pi^*$ absorption maxima, ³MLCT emission maxima, estimated quantum yields, time constants, and ascorbate quenching constants for the $[Ru(L)_3]^{2+}$ and Ru(L)NiRd series.

L =	dmabpy	meob	dmb	dtbub	bpy	phen	dcbpy	btfmb
$[Ru(L)_3]^{2+}$								
λabs,max (π->π*) (nm)	262	275	286	288	286	262	308	293
λ _{abs,max} (MLCT) (nm)	519	477	460	460	452	447	469	456
λ _{em,max} (³ MLCT) (nm)	690	659	619	617	605	592	627	611
PL Quantum Yield (%)	0.06	0.18	2.35	1.36	4.20	6.44	7.85	5.80
$ au_0$ (ns)	48 ± 0.4	61 ± 0.08	320 ± 0.4	429 ± 1.0	588 ± 0.4	805 ± 1	895 ± 2	754 ± 1
k _q (M-1 s-1)	1.80 x 10 ⁶	2.49 x 10 ⁶	2.70 x 10 ⁶	1.69 x 10 ⁶	3.39 x 10 ⁷	2.88 x 108	2.01 x 10 ⁹	2.18 x 10 ⁸
K _S (M ⁻¹)	0.27	0.46	4.9	4.0	1.1			
$k_q \tau_0 / K_S^a$	0.34	0.35	0.14	0.17	14			
Ru(L)NiRd								
λabs,max (π->π*) (nm)	268	276	283	286	285	264	298	292
λ _{abs,max} (MLCT) (nm)	520	457	457	454	454	452	461	457
λ _{em,max} (³ MLCT) (nm)	676	657	626	618	616	614	622	629

complex, a luminescence signal assigned to the spin-forbidden ³MLCT state was observed (Figure S6, **Table 1**, Table S3). Emission spectra recorded at 77 K were used to obtain the E₀₀ value for each complex (Figure S4). Most of the Ru complexes remained highly emissive at room temperature, although the luminescence intensities and corresponding emission quantum yields were significantly lower for [Ru(dmabpy)₃]²⁺, [Ru(meob)₃]²⁺, and [Ru(dmabpy)₂(epoxy-phen)]²⁺ (**Table 1**; Figure S6). TCSPC luminescence lifetime experiments on the $[Ru(L)_3]^{2+}$ series show single exponential decay, with the lifetime (τ) of the 3MLCT excited state generally increasing across the series as the substituents shift from electron donating to electron withdrawing (**Table 1**; Figure S7). The [Ru(L)₂(epoxy-phen)]²⁺ complexes exhibit biexponential decay, with the amplitude of the longer component generally increasing as the substituent becomes more electron withdrawing (Figure S8, Table S4). Stern-Volmer quenching analyses of the emission intensity and the lifetimes across the $[Ru(L)_3]^{2+}$ series show that ascorbate predominantly quenches the ³MLCT excited state through a dynamic quenching mechanism, as the lifetime varies linearly with ascorbate concentration (Figure S9). However, as deviations between I_0/I and τ_0/τ values suggest additional contributions from static quenching with the unsubstituted ligand and those with electron donating substituents,44 lifetime measurements were used to obtain the bimolecular quenching rate constants ranging from 106 to 109 M⁻¹s⁻¹, with values that decrease with increased electron donation from the substituent.48

Electrochemistry of [Ru(L)₃]²⁺

Cyclic voltammetry (CV) was used to determine the relevant reduction potentials for the $[Ru(L)_3]^{2+}$ complexes (Figure S10, Table S5). Each complex undergoes one reversible metal-centered oxidation with formation of the $[Ru(L)_3]^{3+}$ state $(Ru^{3+/2+}$ redox couple) (Figure S11, Table S5). Multiple ligand-centered reduction processes of the bipyridine ligands are also observed, the first of which forms the $[Ru(L)_2(L^-)]^+$ state $(Ru^{2+/+}$ redox couple). Both $[Ru(phen)_3]^{2+}$ and $[Ru(dtbub)_3]^{2+}$ complexes show a large peak near the ligand-centered reduction, suggesting two-electron oxidation back to the Ru^{2+} state. Both the $Ru^{3+/2+}$ and $Ru^{2+/+}$ redox couples are strongly correlated with the substituent Hammett parameters, impacting the corresponding excited state reduction potentials (Table S6). The $[Ru(L)_3]^{2+}$ series was used to approximate the $[Ru(L)_2(epoxy-phen)]^{2+}$ potentials due to the irreversible reduction of the epoxide moiety around -900 mV vs NHE (Figure S12). $^{21.51}$

The E_{00} values and redox potentials of the $[Ru(L)_3]^{2+}$ series were used to generate modified Latimer diagrams for the Ru(L)NiRd constructs to determine the free energies of

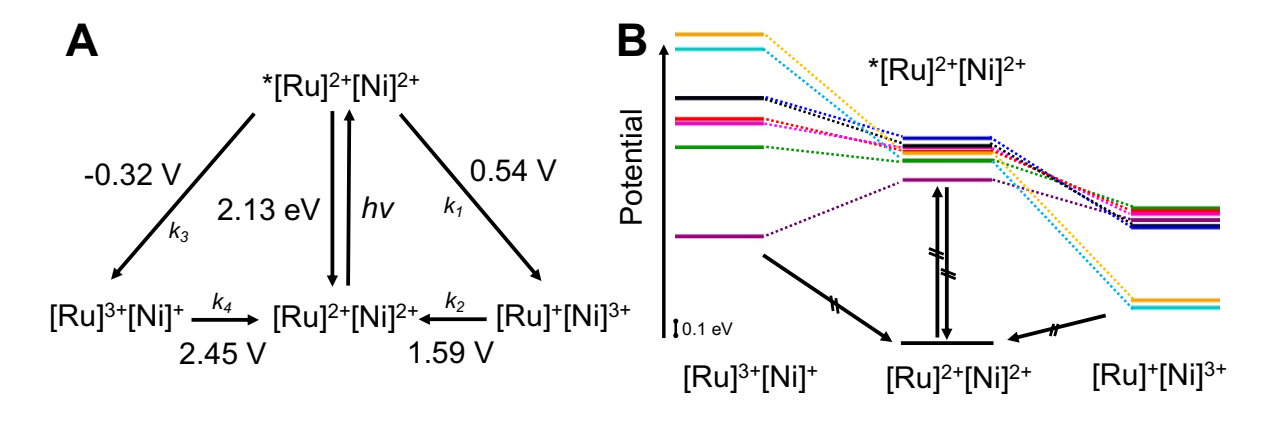


Figure 2. Modified Latimer diagrams for photoinduced electron transfer for (**A**) Ru(bpy)NiRd and (**B**) all Ru(L)NiRd constructs colored as indicated in Figure 1. Reduction potentials for NiRd and Ru(L) are taken from ref. 32 and Table ST5.

intramolecular photoinduced ET processes (**Figure 2**, Figure S13). This analysis predicts that the most electron donating substituents could enable formation of the [Ru]³⁺[Ni]⁺ intermediate, while the electron withdrawing substituents strictly favor the [Ru]⁺[Ni]³⁺ species.

Emission measurements of the Ru(L)NiRd series suggest intramolecular charge transfer

Each Ru phototrigger was covalently attached to the endogenous non-coordinating C31 residue near the active site of the protein, as previously described,^{36,37} with the d->d charge

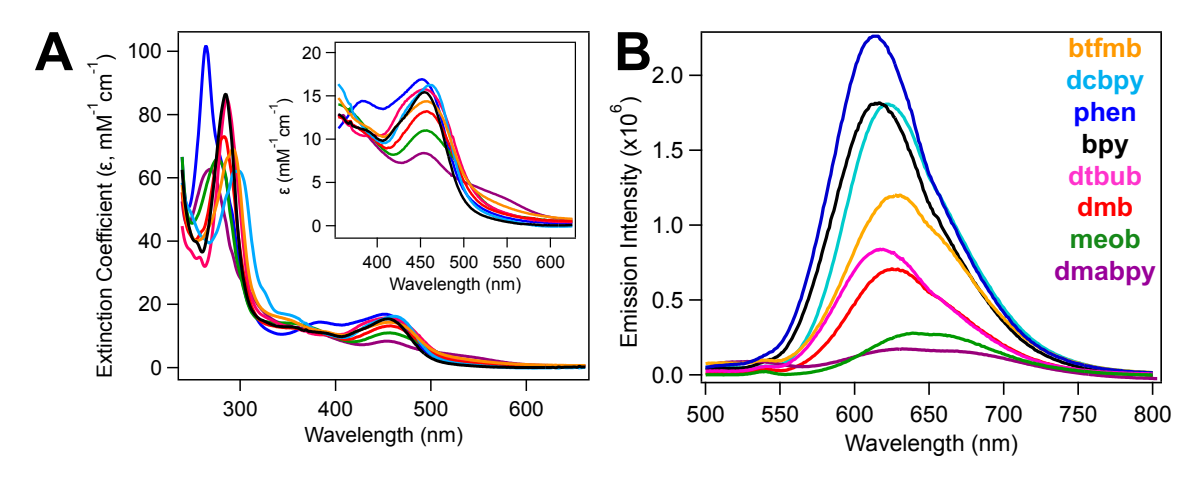


Figure 3. (**A**) Absorption spectra (*Inset*: Zoomed in view of M-L charge transfer region) and (**B**) emission spectra of Ru(L)NiRd constructs (colored as indicated in **B**).

transfer transitions used to verify that the protein remained metalated and electronic structure of the active site unchanged (Figure S14). The UV-vis and emission spectra of the Ru(L)NiRd complexes show the same trends as in the $[Ru(L)_3]^{2+}$ and $[Ru(L)_2(epoxy-phen)]^{2+}$ series (**Figure 3**, **Table 1**, Table S7).

The TCSPC emission lifetimes across the Ru(L)ZnRd series follow biexponential decay, with comparable lifetimes to the $[Ru(L)_2(epoxy-phen)]^{2+}$ series (Table S8), suggesting the protein scaffold does not directly quench the *Ru^{II} excited state. In most cases, the Ru(L)FeRd and

Ru(L)NiRd constructs exhibit an additional, fast decay component (τ_1) that has been previously assigned to intramolecular charge transfer between the metal centers for L = bpy (**Figure 4**, Figure S16, Table S8).³⁷ For Ru(L)FeRd, the values for τ_1 increase from 2 – 18 ns as the *para*-substituent becomes more electron withdrawing (Table S8). For Ru(L)NiRd, on the other hand, the values for this short τ_1 component range from 4 – 22 ns and decrease as the substituent becomes either more electron donating or electron withdrawing relative to bpy. Very short lifetimes overall are observed for Ru(dmabpy)NiRd and Ru(meob)NiRd, precluding resolution of τ_1 for Ru(dmabpy)NiRd and Ru(dmabpy)FeRd.

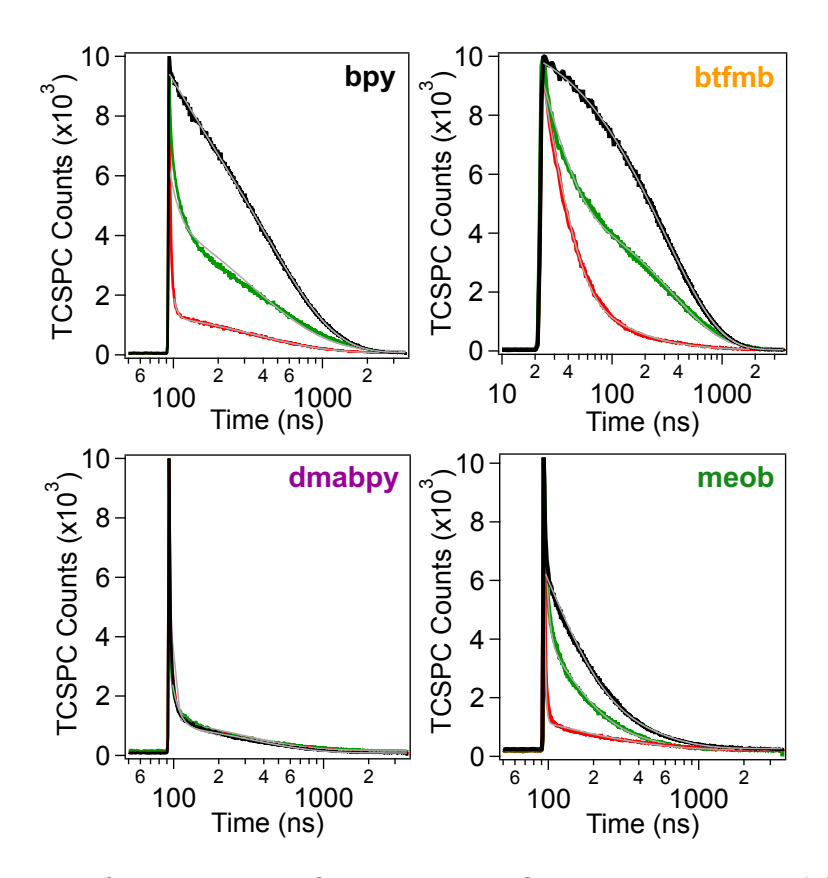


Figure 4. TCSPC luminescence decay traces of representative Ru(L)ZnRd (*black*), Ru(L)FeRd (*red*), and Ru(L)NiRd (*green*) complexes in 1 M phosphate buffer, pH 6.5. Best-fit traces are overlaid (*grey*).

Charge transfer directionality within $\operatorname{Ru}(L)\operatorname{NiRd}$ investigated through nanosecond transient absorption spectroscopy

The modified Latimer diagram (**Figure 2**) indicates that the $[Ru]^{3+}[Ni]^+$ intermediate should be formed in the case of L = dmabpy, which would be expected to be observed at approximately 410 nm.⁵² However, though nanosecond TA experiments performed from 355 nm – 525 nm show the typical positive absorptive features from the 3MLCT state of the Ru(II) complex

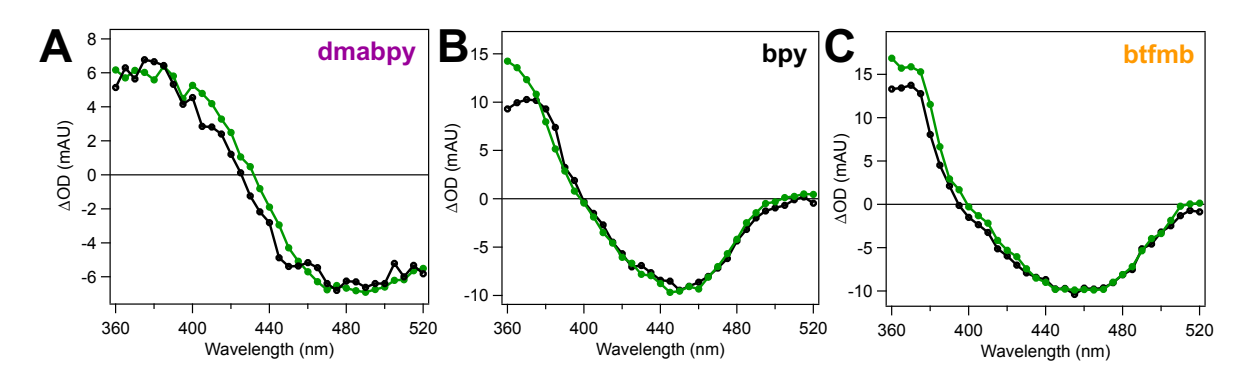


Figure 5. Representative TA spectra of Ru(L)NiRd (*green*) and Ru(L)ZnRd (*black*) in 1 M phosphate buffer, pH 6.5, measured 20 ns after excitation, for L = (A) dmabpy, (B) bpy, and (C) btfmb, as labeled.

associated with the reduced bpy ligand at ~370 nm and the ground state bleach at ~450 nm, no significant spectral differences between the Ru(L)NiRd and Ru(L)ZnRd spectra were noted (**Figure 5**, Figure S17).

A closer look at the transient kinetic traces at 520 nm reveals a positive absorption feature

when L = bpy, dcbpy, and btfmb (**Figure 6**, Figure S18), with a lifetime that increases as the substituents become more electron-withdrawing (Figure S19, Table S9). This feature is attributed to charge transfer from Ni^{2+} to Ru^{2+} , as it matches the spectroscopic signature of $[Ru]^{+37}$ and is not observed when M = Zn, Fe nor with any electron donating substituents. The slight, persistent absorption offset evident at 520 nm for Ru(dmabpy)Rd and Ru(dcbpy)NiRd may arise from slight photoinduced changes around the

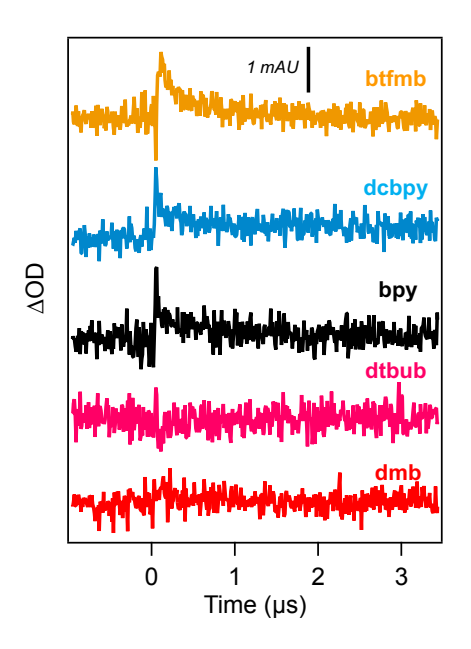


Figure 6. TA difference traces at 520 nm of Ru(L)NiRd – Ru(L)ZnRd, normalized to the amount of Ru^{II} bleach. Samples contained approximately 50 μM Ru(L)MRd and were measured in 1 M phosphate

ruthenium binding site within rubredoxin, consistent with slight variations in the absorption spectra around $^{\sim}740$ nm. We note that these are the two substituents imparting a charge to the bpy ligand, which may introduce additional interactions. Across the Ru(L)ZnRd and Ru(L)NiRd series, the single-wavelength kinetics at 370 nm and 450 nm are similar to those measured from the emission decays (Table S10, Figure S20-S21), indicating that the observed ground state bleach originates from the 3 MLCT state. As the transient absorption spectra of Ru(L)ZnRd are similar to those of [RuL₃]²⁺ for L = bpy, the excited state has been suggested to be localized on the bpy ligands rather than the cysteine-bound dihydrophenanthroline

ligand.³⁷ Processes faster than the 10-ns instrument response time could not be resolved in TA experiments.

Photodriven hydrogen evolution correlates with driving force

To connect the nano-to-microsecond timescale experiments with the slower catalytic processes and elucidate how the photophysical and photochemical properties of the ruthenium phototrigger impact the overall hydrogen evolution activity, light-driven assays were performed on the Ru(L)NiRd series. Hydrogen evolution was monitored using gas chromatography (GC) analysis. Ascorbate was used as the sacrificial electron donor, and

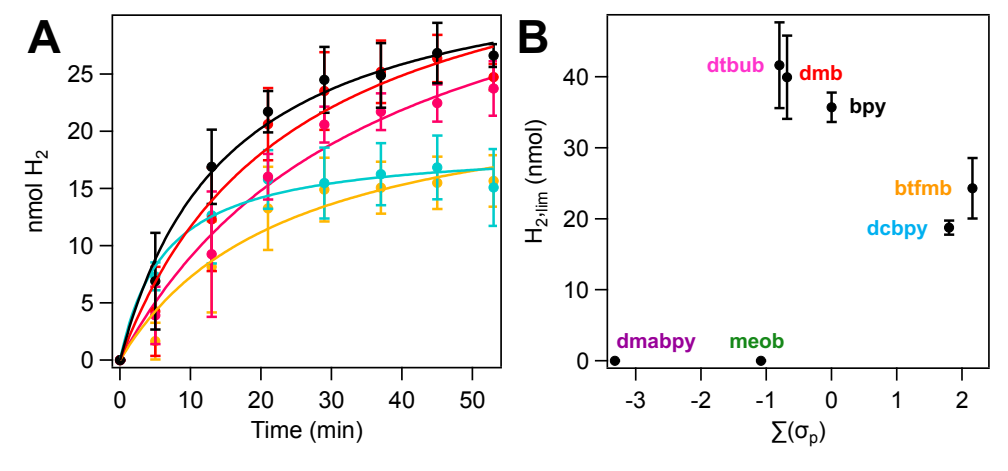


Figure 7. (A) Light-driven hydrogen evolved by 10 μM Ru(L)NiRd in 1 M phosphate, pH 6.5, with 100 mM ascorbate at defined time points (circles). Fits modeled with Michaelis-Menton kinetics are shown as lines. (B) Results of Ru(L)NiRd GC assays showing maximum limiting amount of H₂ produced plotted against Hammett parameters for L as evolved H₂ gas in the headspace was measured at defined time points. Ru(bpy)NiRd, Ru(dmb)NiRd, Ru(dtbub)NiRd, Ru(btfmb)NiRd, and Ru(dcbpy)NiRd are all active for hydrogen evolution under the tested conditions with varying catalytic rates, while no hydrogen was observed with Ru(meob)NiRd, Ru(dmabpy)NiRd, or Ru(phen)NiRd (Figure 7A). Varying pH, quencher concentration, excitation wavelength, or using BNAH as the

sacrificial electron donor did not result in hydrogen gas being produced by Ru(dmabpy)NiRd. We note that Ru(bpy)NiRd is active for hydrogen evolution with BNAH as a sacrificial electron donor (Figure S22), albeit with lower turnover than observed with ascorbate. As previously reported, all covalently attached constructs produced more hydrogen than assays containing a stoichiometric mixture of [Ru(L)₃]²⁺ and NiRd (Figure S23).³⁶ Hydrogen evolution activity was modeled with Michaelis-Menton kinetics⁵³ and found to correlate with the electron donating ability of the substituent, contingent on observation of any photodriven activity (**Figure 7B**).

DISCUSSION

Bipyridine substituents perturb ground and excited state properties of the ruthenium phototrigger independent of the NiRd catalytic site

The photophysical and electrochemical properties of the ruthenium phototrigger report on the ground and excited state properties of the complex (**Figure 8A**), suggesting that an increase in electron donation from the para-substituent reduces π -backbonding and destabilizes the $d\pi$ orbitals, raising their energy (**Figure 8B**). This effect has been observed in other studies on modified Ru bipyridine complexes,^{41,54} where a slight decrease in the MLCT energy with electron withdrawing substituents reflects a small decrease in the low-lying π^* energy level of the ligands. The bimolecular quenching rate constants also show a strong correlation with the excited state reduction potential (**Figure 8C**). These types of linear free energy relationships

have been previously observed; however, they do not fully explain the hydrogen evolution behavior across the Ru(L)NiRd series, as discussed further below.

In contrast to the systematic modulation of the phototrigger properties across this series, the

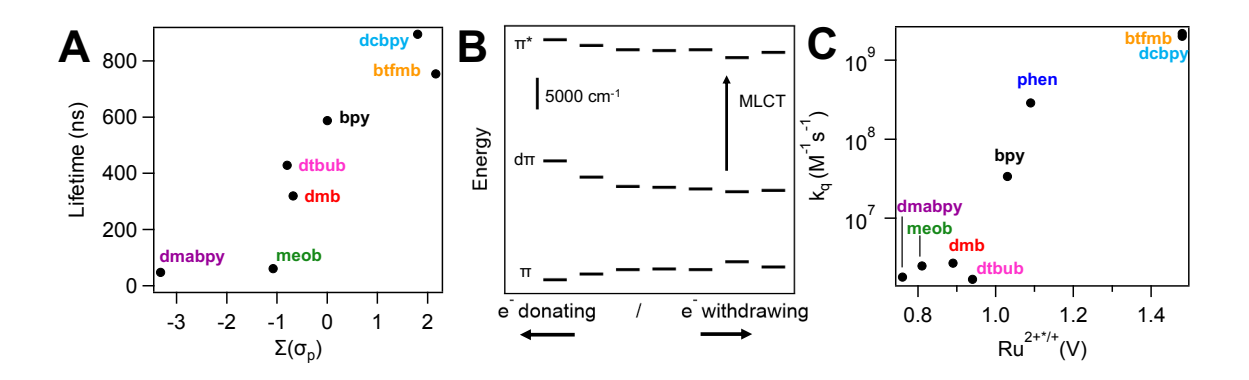


Figure 8. (**A**) Lifetime of ${}^*[Ru(L)_3]^{2+}$ vs. Hammett parameters. (**B**) Semi-quantitative partial MO diagram illustrating the effect of the substituents on the orbital energies of $[Ru(L)_3]^{2+}$. (**C**) Bimolecular quenching constants between ${}^*[Ru(L)_3]^{2+}$ and ascorbate relative to the experimentally determined $Ru^{2+7/+}$ couple.

catalytic NiRd active site remains unchanged (Figure S14), highlighting an advantage of using a protein as a scaffold; the structure decouples the electronic properties of the phototrigger from the catalyst. While the ruthenium and nickel are in sufficiently close proximity to promote intramolecular electron transfer (*vide infra*), the properties of each can be tuned independently, suggesting orthogonal routes for global system optimization.

Time-resolved spectroscopy reveals long-lived, charge-separated species

Direct reductive and oxidative quenching of the *Ru^{II} excited state by Ni and Fe, respectively, is observed from TSCPC lifetime measurements across all Ru(L)FeRd and Ru(L)NiRd constructs, except for the Ru(dmabpy)MRd series, where this additional component may lie

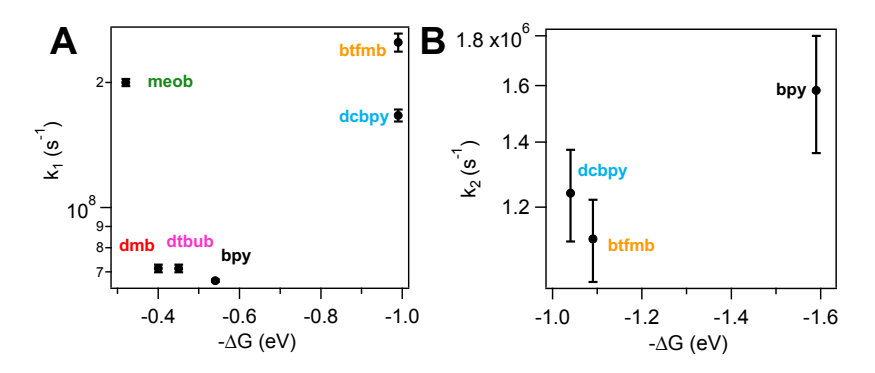


Figure 9. (**A**) Rates of forward, excited-state electron transfer, k_1 , determined through TCPSC experiments as a function of the driving force for forming the $[Ru]^+[Ni]^{3+}$ state. (**B**) Rates of back electron transfer, k_2 , determined through transient absorption experiments as a function of the driving force for regenerating the $[Ru]^{2+}[Ni]^{2+}$ state.

within the time resolution of the instrument (**Figure 4**, Table S8). The rates (k₁) for forward ET generally increase with driving force for formation of the [Ru]*[Ni]³⁺ state (**Figure 9A**). The anomalously high rates observed for L = meob suggest that both oxidative and reductive quenching may be operative with this substituent, as both pathways are thermodynamically accessible (**Figure 2B**). While direct spectroscopic evidence of the [Ru]³⁺[Ni]* intermediate was not observed through nanosecond TA spectroscopy (**Figure 5**, Figure S17), the [Ru]³⁺ absorption feature is anticipated to appear around 410 nm with a low extinction coefficient, which may be masked by the low signal-to-noise ratios in the experiment.⁵² The dependence of intramolecular quenching rate with driving force roughly agrees with the exponential behavior expected from Marcus theory,⁵⁵ with the monotonic increase indicating the total reorganization energy must be greater than 1 eV.

The back electron transfer from the [Ru]⁺[Ni]³⁺ state to regenerate the ground state can be resolved using TA spectroscopy, with kinetics monitored at 520 nm, for L = bpy, dcbpy, and btfmb (**Figure 6**, Figure S19). These rates are much more similar across the three constructs

but increase slightly with increased driving force, suggesting a lower bound for reorganization energy of ~1.6 eV. Forming the oxidized [Ni]³+ center in Rd is anticipated to be associated with large reorganization energies, given the distinct coordination preferences between [Ni]²+ and [Ni]³+ centers. These experiments provide the framework to begin to resolve this information, though access to a larger dynamic range in driving force will be required. Nonetheless, the extremely rapid forward ET accompanied by slow recombination indicates formation of a long-lived, charge-separated state, analogous to the highly efficient charge separation seen in photosynthesis. This lifetime can be stabilized through tuning the potentials for each ET process, which can guide the design of such motifs in synthetic solar fuels systems.

A multivariate approach is necessary to optimize solar fuel production

The underlying hypothesis for this study was that increasing the driving force for formation of the putative catalytic [Ru]³⁺[Ni]⁺ intermediate, by increasing electron donation on the ruthenium phototrigger, would increase the amount of hydrogen produced by Ru(L)NiRd in a systematic manner. This hypothesis was partially validated, as among the five catalytically active constructs, a correlation was indeed observed between the electron-donating ability of the substituted phototrigger and the amount of hydrogen gas formed (Figure 7B). The lessons from these systems may be leveraged to take advantage of known photophysical and photochemical properties for rational optimization of functional systems for solar fuel production. However, the most electron-donating systems, Ru(dmabpy)NiRd and Ru(meob)NiRd, were completely inactive towards photodriven hydrogen evolution, which has been attributed to a combination of short excited-state lifetimes due to rapid non-radiative

quenching and slow, unproductive reductive quenching. Although static quenching does appear to dominate over dynamic quenching in the L= dmabpy and L= meob systems (**Table** 1), this is also the case for constructs that show high levels of hydrogen production activity (e.g., L= dmb and L= dtbub), necessitating an alternative explanation for the lack of hydrogen produced. The increase in hydrogen gas production with increased electron donation into the bpy ligands also cannot simply be attributed to quenching rates, as the quenching rate constants were found to correlate strongly with driving force for formation of the $[Ru]^+$ species and thus inversely with the electron donating ability (**Figure 8C**, Figure S24). Therefore, we postulate that the increased driving force for the formation of the $[Ru]^{3+}[Ni]^+$ species contributes to the hydrogen evolution capabilities of the NiRd enzyme, even though this species does not accumulate to such an extent that it can be observed spectroscopically.

Despite the wide range of excited state reduction potentials accessed, the differences in activity across the series are only modest. This observation underscores the intricacies involved in designing an artificial enzyme in which multiple electron and proton transfer steps must be coordinated. This work has primarily addressed phototrigger attributes contributing to initial formation of the catalyst reduced state, i.e., PSCAT⁻ relative to PS⁺CAT⁻ (**Figure 1A**). This study reveals that the bimolecular reductive quenching pathway is not solely responsible for driving catalysis, though it does remain dominant. While the inactivity of Ru(dmabpy)NiRd and Ru(meob)NiRd can be understood in the context of excited-state lifetime and quenching rate, Ru(phen)NiRd is also inactive for hydrogen evolution, despite exhibiting a long excited-state lifetime and a high quenching rate constant. We consider that the charge density of both the

excited state and the reduced, quenched phototrigger may also play a role in modulating activity. For L = phen, charge transfer in the excited state may be delocalized across the phenanthroline ligands, lowering the propensity for productive ET to the nickel center.⁵⁶ Rapid back ET also cannot be ruled out. As phenanthroline ligands can be readily modified, 57,58 future studies may focus on using substituted phenanthroline ligands to drive localization of the excited state towards the protein, and we hypothesize that varying the energetics of these ligands can be used to restore ET to the nickel center. For L = btfmb and L = dcbpy, the reduced state may be localized away from the protein-bound bipyridine ligand, changing the electron transfer pathway between the phototrigger and the catalytic site and likely decreasing the intramolecular ET rate. This may also contribute to the decrease in activity for these systems. Beyond thermodynamic considerations for forming a catalytically relevant intermediate, the rates of each subsequent elementary step in catalysis must be considered, as they also contribute to the overall activity of the artificial enzyme. At present, these steps are masked. The divergent timescales of intramolecular ET processes and H2 formation obscure observation of catalytic intermediates other than the rapidly formed one-electron reduced species, because species that are slow to form do not accumulate. Future work may take advantage of sequential photoexcitation experiments coupled with mixing steps to probe downstream intermediates formed during catalysis. At present, the measurement of total H₂ produced provides a proxy for the overall efficiency of the downstream processes, which, from this work, can be

decoupled from the initial reduction step. It is apparent that, despite the slight improvement

in catalysis based on ET driving force, the rational optimization of an artificial enzymephotosensitizer construct requires consideration of a multitude of interacting factors.

This study provides a new approach in the growing field of artificial metalloenzyme design, one that capitalizes on the method of initiating catalysis, which was met with modest success. The Ru(L)NiRd constructs complement a body of work using NiRd as a platform for an artificial hydrogenase that includes generating a large library of secondary sphere mutants,⁵⁹ choosing rubredoxin sequences from diverse organisms, 60 developing active site mutants, and performing computational studies.⁶¹ These prior studies have driven stepwise, onedimensional improvements to the system. However, the data presented here contribute to an increasingly rich database on NiRd and other artificial metalloenzymes relating well-defined molecular factors to activity. As machine learning algorithms become better equipped to manage what is still sparse data, we believe these tools may offer a powerful complement to the rational design approach pursued in this and prior work. Ultimately, given the complex dependence of activity across a number of competing factors, as illustrated in this work, these artificial intelligence strategies may facilitate multivariate optimization of artificial metalloenzymes for small molecule activation and solar fuel production.

CONCLUSIONS

In this work, we modulated the light-driven H₂ evolution activity of the artificial metalloenzyme Ru(L)NiRd by systematically tuning the *para*-substituent on covalently attached ruthenium complexes. Investigation of photophysical properties connected the

behavior of the free photosensitizer in aqueous solution to those of the covalently attached complexes. Gas chromatography assays revealed a correlation between the electron donating ability of the substituent and the amount of hydrogen gas evolved, highlighting the significance of tuning the driving force for catalytic activity. However, photophysical factors beyond driving force, such as lifetime and quenching rates, also had a substantial impact on activity, dominating the observed catalytic performance in some constructs. This study underscores the complexity of optimizing artificial enzyme-photosensitizer constructs and emphasizes the need to understand the interplay between the many factors influencing multistep catalysis.

ASSOCIATED CONTENT

The following files are available free of charge.

Supplemental figures and tables (PDF): Supplemental figures showing synthetic schemes, the labeling procedure for Ru(L)MRd, optical spectra, fits for TCSPC measurements, cyclic voltammograms, and the modified Latimer diagram for the Ru(L)NiRd series.

AUTHOR INFORMATION

Corresponding Authors

*Dr. Hannah Shafaat, shafaat@ucla.edu

*Dr. Claudia Turro, turro.1@osu.edu

Author Contributions

The manuscript was written through contributions of all authors. All authors have given approval to the final version of the manuscript.

Funding Sources

H.S.S., A.E.W., and S.C.M. would like to thank the U.S. National Science Foundation for supporting this research (CHE-1454289, CHE-2108684, CHE-2419343). C.T. gratefully acknowledges the partial support of the National Science Foundation (CHE-2102508).

ACKNOWLEDGMENTS

A.E.W. would like to thank the members of the Turro group for helpful discussions and training on instrumentation.

REFERENCES

- (1) Billewar, S. R.; Londhe, G.; Mane, P. S. World Energy Demand. In *Integrated Green Energy Solutions Volume 2*; John Wiley & Sons, Ltd, 2023; pp 275–316. https://doi.org/10.1002/9781394193738.ch36.
- (2) Pourasl, H. H.; Barenji, R. V.; Khojastehnezhad, V. M. Solar Energy Status in the World: A Comprehensive Review. *Energy Reports* 2023, 10, 3474–3493. https://doi.org/10.1016/j.egyr.2023.10.022.
- (3) Kabir, E.; Kumar, P.; Kumar, S.; Adelodun, A. A.; Kim, K.-H. Solar Energy: Potential and Future Prospects. *Renewable and Sustainable Energy Reviews* **2018**, *82*, 894–900. https://doi.org/10.1016/j.rser.2017.09.094.

- (4) Gray, H. B. Powering the Planet with Solar Fuel. *Nature Chem* **2009**, *I* (1), 7–7. https://doi.org/10.1038/nchem.141.
- (5) Nocera, D. G. Solar Fuels and Solar Chemicals Industry. *Acc. Chem. Res.* **2017**, *50* (3), 616–619. https://doi.org/10.1021/acs.accounts.6b00615.
- (6) Yoshitomi, F.; Sekizawa, K.; Maeda, K.; Ishitani, O. Selective Formic Acid Production via CO2 Reduction with Visible Light Using a Hybrid of a Perovskite Tantalum Oxynitride and a Binuclear Ruthenium(II) Complex. ACS Appl. Mater. Interfaces 2015, 7 (23), 13092– 13097. https://doi.org/10.1021/acsami.5b03509.
- (7) Haussener, S. Solar Fuel Processing: Comparative Mini-Review on Research, Technology Development, and Scaling. *Solar Energy* 2022, 246, 294–300. https://doi.org/10.1016/j.solener.2022.09.019.
- (8) Hammarström, L. Accumulative Charge Separation for Solar Fuels Production: Coupling Light-Induced Single Electron Transfer to Multielectron Catalysis. *Acc. Chem. Res.* 2015, 48 (3), 840–850. https://doi.org/10.1021/ar500386x.
- (9) Morris, A. J.; Meyer, G. J.; Fujita, E. Molecular Approaches to the Photocatalytic Reduction of Carbon Dioxide for Solar Fuels. *Acc. Chem. Res.* 2009, 42 (12), 1983–1994. https://doi.org/10.1021/ar9001679.
- (10) Sun, K.; Moreno-Hernandez, I. A.; Schmidt, W. C.; Zhou, X.; Crompton, J. C.; Liu, R.; Saadi, F. H.; Chen, Y.; Papadantonakis, K. M.; Lewis, N. S. A Comparison of the Chemical, Optical and Electrocatalytic Properties of Water-Oxidation Catalysts for Use in Integrated Solar-Fuel Generators. *Energy Environ. Sci.* 2017, 10 (4), 987–1002. https://doi.org/10.1039/C6EE03563A.

- (11) Trimble, J. S.; Crawshaw, R.; Hardy, F. J.; Levy, C. W.; Brown, M. J. B.; Fuerst, D. E.; Heyes, D. J.; Obexer, R.; Green, A. P. A Designed Photoenzyme for Enantioselective [2+2] Cycloadditions. *Nature* **2022**, *611* (7937), 709–714. https://doi.org/10.1038/s41586-022-05335-3.
- (12) Teegardin, K.; Day, J. I.; Chan, J.; Weaver, J. Advances in Photocatalysis: A Microreview of Visible Light Mediated Ruthenium and Iridium Catalyzed Organic Transformations. *Org. Process Res. Dev.* 2016, 20 (7), 1156–1163. https://doi.org/10.1021/acs.oprd.6b00101.
- (13) Melchionna, M.; Fornasiero, P. Updates on the Roadmap for Photocatalysis. *ACS Catal.* **2020**, *10* (10), 5493–5501. https://doi.org/10.1021/acscatal.0c01204.
- (14) Eckenhoff, W. T.; Eisenberg, R. Molecular Systems for Light Driven Hydrogen Production. *Dalton Trans.* **2012**, *41* (42), 13004–13021. https://doi.org/10.1039/C2DT30823A.
- (15) Millet, A.; Xue, C.; Turro, C.; Dunbar, K. R. Unsymmetrical Dirhodium Single Molecule Photocatalysts for H₂ Production with Low Energy Light. *Chem. Commun.* **2021**, *57* (16), 2061–2064. https://doi.org/10.1039/D0CC08248A.
- (16) Gong, L.; Yin, H.; Nie, C.; Sun, X.; Wang, X.; Wang, M. Influence of Anchoring Groups on the Charge Transfer and Performance of P-Si/TiO2/Cobaloxime Hybrid Photocathodes for Photoelectrochemical H2 Production. ACS Appl. Mater. Interfaces 2019, 11 (37), 34010– 34019. https://doi.org/10.1021/acsami.9b12182.
- (17) Roth, L. E.; Nguyen, J. C.; Tezcan, F. A. ATP- and Iron-Protein-Independent Activation of Nitrogenase Catalysis by Light. J. Am. Chem. Soc. 2010, 132 (39), 13672–13674. https://doi.org/10.1021/ja1071866.
- (18) Vansuch, G. E.; Mulder, D. W.; Chica, B.; Ruzicka, J. L.; Yang, Z.-Y.; Pellows, L. M.; Willis, M. A.; Brown, K. A.; Seefeldt, L. C.; Peters, J. W.; Dukovic, G.; King, P. W. Cryo-

- Annealing of Photoreduced CdS Quantum Dot–Nitrogenase MoFe Protein Complexes Reveals the Kinetic Stability of the E4(2N2H) Intermediate. *J. Am. Chem. Soc.* **2023**, *145* (39), 21165–21169. https://doi.org/10.1021/jacs.3c06832.
- (19) Pizano, A. A.; Lutterman, D. A.; Holder, P. G.; Teets, T. S.; Stubbe, J.; Nocera, D. G. Photo-Ribonucleotide Reductase B2 by Selective Cysteine Labeling with a Radical Phototrigger. Proceedings of the National Academy of Sciences 2012, 109 (1), 39–43. https://doi.org/10.1073/pnas.1115778108.
- (20) Mendoza, V. L.; Vachet, R. W. Probing Protein Structure by Amino Acid-Specific Covalent Labeling and Mass Spectrometry. *Mass Spectrometry Reviews* **2009**, *28* (5), 785–815. https://doi.org/10.1002/mas.20203.
- (21) Dwaraknath, S.; Tran, N.-H.; Dao, T.; Colbert, A.; Mullen, S.; Nguyen, A.; Cortez, A.; Cheruzel, L. A Facile and Versatile Methodology for Cysteine Specific Labeling of Proteins with Octahedral Polypyridyl D6 Metal Complexes. *Journal of Inorganic Biochemistry* 2014, 136, 154–160. https://doi.org/10.1016/j.jinorgbio.2013.12.013.
- (22) Winkler, J. R.; Gray, H. B. *Electron transfer in ruthenium-modified proteins*. ACS Publications. https://doi.org/10.1021/cr00011a001.
- (23) Ennist, N. M.; Stayrook, S. E.; Dutton, P. L.; Moser, C. C. Rational Design of Photosynthetic Reaction Center Protein Maquettes. *Front. Mol. Biosci.* 2022, 9. https://doi.org/10.3389/fmolb.2022.997295.
- (24) Chalker, J. M.; Bernardes, G. J. L.; Lin, Y. A.; Davis, B. G. Chemical Modification of Proteins at Cysteine: Opportunities in Chemistry and Biology. *Chemistry An Asian Journal* **2009**, *4* (5), 630–640. https://doi.org/10.1002/asia.200800427.

- (25) Utterback, J. K.; Ruzicka, J. L.; Keller, H. R.; Pellows, L. M.; Dukovic, G. Electron Transfer from Semiconductor Nanocrystals to Redox Enzymes. *Annu. Rev. Phys. Chem.* 2020, 71 (1), 335–359. https://doi.org/10.1146/annurev-physchem-050317-014232.
- (26) Brown, K. A.; Dayal, S.; Ai, X.; Rumbles, G.; King, P. W. Controlled Assembly of Hydrogenase-CdTe Nanocrystal Hybrids for Solar Hydrogen Production. *J. Am. Chem. Soc.* 2010, 132 (28), 9672–9680. https://doi.org/10.1021/ja101031r.
- (27) Angerani, S.; Winssinger, N. Visible Light Photoredox Catalysis Using Ruthenium Complexes in Chemical Biology. *Chemistry A European Journal* **2019**, *25* (27), 6661–6672. https://doi.org/10.1002/chem.201806024.
- (28) Liu, Y.; Hammitt, R.; Lutterman, D. A.; Joyce, L. E.; Thummel, R. P.; Turro, C. Ru(II)

 Complexes of New Tridentate Ligands: Unexpected High Yield of Sensitized 1O2. *Inorg. Chem.* **2009**, *48* (1), 375–385. https://doi.org/10.1021/ic801636u.
- (29) Dunbar, M. N.; Steinke, S. J.; Piechota, E. J.; Turro, C. Differences in Photophysical Properties and Photochemistry of Ru(II)–Terpyridine Complexes of CH3CN and Pyridine. *J. Phys. Chem. A* **2024**, *128* (3), 599–610. https://doi.org/10.1021/acs.jpca.3c07432.
- (30) Thompson, D. W.; Ito, A.; Meyer, T. J. [Ru(bpy)3]2+* and other remarkable metal-to-ligand charge transfer (MLCT) excited states. *Pure and Applied Chemistry* **2013**, *85* (7), 1257–1305. https://doi.org/10.1351/PAC-CON-13-03-04.
- (31) Masaoka, S.; Mukawa, Y.; Sakai, K. Frontier Orbital Engineering of Photo-Hydrogen-Evolving Molecular Devices: A Clear Relationship between the H2-Evolving Activity and the Energy Level of the LUMO. *Dalton Trans.* 2010, 39 (25), 5868–5876. https://doi.org/10.1039/C0DT00077A.

- (32) Suneesh, C. V.; Balan, B.; Ozawa, H.; Nakamura, Y.; Katayama, T.; Muramatsu, M.; Nagasawa, Y.; Miyasaka, H.; Sakai, K. Mechanistic Studies of Photoinduced Intramolecular and Intermolecular Electron Transfer Processes in RuPt-Centred Photo-Hydrogen-Evolving Molecular Devices. *Phys. Chem. Chem. Phys.* 2013, *16* (4), 1607–1616. https://doi.org/10.1039/C3CP54630F.
- (33) Lubitz, W.; Ogata, H.; Rüdiger, O.; Reijerse, E. Hydrogenases. *Chem. Rev.* **2014**, *114* (8), 4081–4148. https://doi.org/10.1021/cr4005814.
- (34) Slater, J. W.; Shafaat, H. S. Nickel-Substituted Rubredoxin as a Minimal Enzyme Model for Hydrogenase. *J. Phys. Chem. Lett.* **2015**, *6* (18), 3731–3736. https://doi.org/10.1021/acs.jpclett.5b01750.
- (35) Slater, J. W.; Marguet, S. C.; Monaco, H. A.; Shafaat, H. S. Going beyond Structure: Nickel-Substituted Rubredoxin as a Mechanistic Model for the [NiFe] Hydrogenases. *J. Am. Chem. Soc.* **2018**, *140* (32), 10250–10262. https://doi.org/10.1021/jacs.8b05194.
- (36) Stevenson, M. J.; Marguet, S. C.; Schneider, C. R.; Shafaat, H. S. Light-Driven Hydrogen Evolution by Nickel-Substituted Rubredoxin. *ChemSusChem* 2017, 10 (22), 4424–4429. https://doi.org/10.1002/cssc.201701627.
- (37) Marguet, S. C.; Stevenson, M. J.; Shafaat, H. S. Intramolecular Electron Transfer Governs Photoinduced Hydrogen Evolution by Nickel-Substituted Rubredoxin: Resolving Elementary Steps in Solar Fuel Generation. *J. Phys. Chem. B* **2019**, *123* (46), 9792–9800. https://doi.org/10.1021/acs.jpcb.9b08048.
- (38) Broomhead, J. A.; Young, C. G.; Hood, P. 29. Tris(2,2'-Bipyridine)Ruthenium(II)

 Dichloride Hexahydrate. In *Inorganic Syntheses*; John Wiley & Sons, Ltd, 1982; pp 127–
 128. https://doi.org/10.1002/9780470132524.ch29.

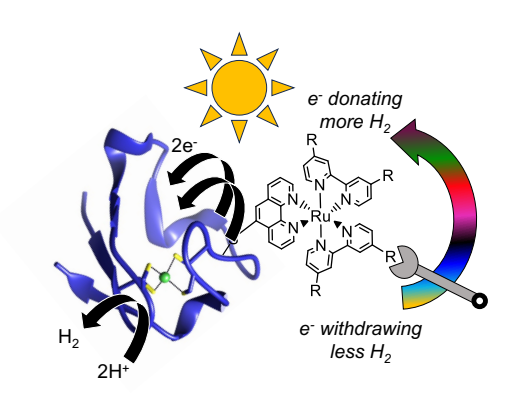
- (39) Rillema, D. P.; Allen, G.; Meyer, T. J.; Conrad, D. Redox Properties of Ruthenium(II) Tris Chelate Complexes Containing the Ligands 2,2'-Bipyrazine, 2,2'-Bipyridine, and 2,2'-Bipyrimidine. *Inorg. Chem.* **1983**, *22* (11), 1617–1622. https://doi.org/10.1021/ic00153a012.
- (40) Viala, C.; Coudret, C. An Expeditious Route to *Cis*-Ru(Bpy)2C12 (Bpy = 2,2'-Bipyridine) Using Carbohydrates as Reducers. *Inorganica Chimica Acta* **2006**, *359* (3), 984–989. https://doi.org/10.1016/j.ica.2005.07.019.
- (41) Shalan, H.; Colbert, A.; Nguyen, T. T.; Kato, M.; Cheruzel, L. Correlating the Para-Substituent Effects on Ru(II)-Polypyridine Photophysical Properties and on the Corresponding Hybrid P450 BM3 Enzymes Photocatalytic Activity. *Inorg. Chem.* 2017, 56 (11), 6558–6564. https://doi.org/10.1021/acs.inorgchem.7b00685.
- (42) Pavlishchuk, V. V.; Addison, A. W. Conversion Constants for Redox Potentials Measured versus Different Reference Electrodes in Acetonitrile Solutions at 25°C. *Inorganica Chimica Acta* 2000, 298 (1), 97–102. https://doi.org/10.1016/S0020-1693(99)00407-7.
- (43) Kautsky, H. Quenching of Luminescence by Oxygen. *Trans. Faraday Soc.* **1939**, *35* (0), 216–219. https://doi.org/10.1039/TF9393500216.
- (44) Quenching of Fluorescence. In *Principles of Fluorescence Spectroscopy*; Lakowicz, J. R., Ed.; Springer US: Boston, MA, 2006; pp 277–330. https://doi.org/10.1007/978-0-387-46312-4_8.
- (45) Balzani, V.; Ceroni, P.; Credi, A.; Venturi, M. Ruthenium Tris(Bipyridine) Complexes: Interchange between Photons and Electrons in Molecular-Scale Devices and Machines. Coordination Chemistry Reviews 2021, 433, 213758. https://doi.org/10.1016/j.ccr.2020.213758.

- (46) Brouwer, A. M. Standards for photoluminescence quantum yield measurements in solution (IUPAC Technical Report). *Pure and Applied Chemistry* **2011**, *83* (12), 2213–2228. https://doi.org/10.1351/PAC-REP-10-09-31.
- (47) Ji, Z.; Huang*, S. D.; Guadalupe*, A. R. Synthesis, X-Ray Structures, Spectroscopic and Electrochemical Properties of Ruthenium(II) Complexes Containing 2,2'-Bipyrimidine. *Inorganica Chimica Acta* **2000**, *305* (2), 127–134. https://doi.org/10.1016/S0020-1693(00)00123-7.
- (48) Gehlen, M. H. The Centenary of the Stern-Volmer Equation of Fluorescence Quenching: From the Single Line Plot to the SV Quenching Map. *Journal of Photochemistry and Photobiology C: Photochemistry Reviews* **2020**, *42*, 100338. https://doi.org/10.1016/j.jphotochemrev.2019.100338.
- (49) Hansch, Corwin.; Leo, A.; Taft, R. W. A Survey of Hammett Substituent Constants and Resonance and Field Parameters. *Chem. Rev.* **1991**, *91* (2), 165–195. https://doi.org/10.1021/cr00002a004.
- (50) Juris, A.; Balzani, V.; Barigelletti, F.; Campagna, S.; Belser, P.; von Zelewsky, A. Ru(II) Polypyridine Complexes: Photophysics, Photochemistry, Eletrochemistry, and Chemiluminescence. *Coordination Chemistry Reviews* 1988, 84, 85–277. https://doi.org/10.1016/0010-8545(88)80032-8.
- (51) Boujlel, K.; Simonet, J. Cathodic Cleavage of Carbon-Oxygen Bonds (V). Direct and Indirect Electrochemical Reduction of Epoxides. *Electrochimica Acta* 1979, 24 (5), 481–487. https://doi.org/10.1016/0013-4686(79)85020-3.

- (52) Tarnovsky, A. N.; Gawelda, W.; Johnson, M.; Bressler, C.; Chergui, M. Photexcitation of Aqueous Ruthenium(II)-Tris-(2,2'-Bipyridine) with High-Intensity Femtosecond Laser Pulses. *J. Phys. Chem. B* **2006**, *110* (51), 26497–26505. https://doi.org/10.1021/jp064696f.
- (53) Johnson, K. A.; Goody, R. S. The Original Michaelis Constant: Translation of the 1913 Michaelis–Menten Paper. *Biochemistry* 2011, 50 (39), 8264–8269. https://doi.org/10.1021/bi201284u.
- (54) Zhou, M.; Robertson, G. P.; Roovers, J. Comparative Study of Ruthenium(II)
 Tris(Bipyridine) Derivatives for Electrochemiluminescence Application. *Inorg. Chem.* 2005, 44 (23), 8317–8325. https://doi.org/10.1021/ic0510112.
- (55) Marcus, R. A. Electron Transfer Reactions in Chemistry Theory and Experiment. *Journal of Electroanalytical Chemistry* **1997**, *438* (1), 251–259. https://doi.org/10.1016/S0022-0728(97)00091-0.
- (56) Turro, C.; Bossmann, S. H.; Leroi, G. E.; Barton, J. K.; Turro, N. J. Ligand-Specific Charge Localization in the MLCT Excited State of Ru(Bpy)2(Dpphen)2+ Monitored by Time-Resolved Resonance Raman Spectroscopy. *Inorg. Chem.* 1994, 33 (7), 1344–1347. https://doi.org/10.1021/ic00085a022.
- (57) Warren, J. T.; Chen, W.; Johnston, D. H.; Turro, C. Ground-State Properties and Excited-State Reactivity of 8-Quinolate Complexes of Ruthenium(II). *Inorg. Chem.* **1999**, *38* (26), 6187–6192. https://doi.org/10.1021/ic991001z.
- (58) Hu, M.-Y.; He, Q.; Fan, S.-J.; Wang, Z.-C.; Liu, L.-Y.; Mu, Y.-J.; Peng, Q.; Zhu, S.-F. Ligands with 1,10-Phenanthroline Scaffold for Highly Regioselective Iron-Catalyzed Alkene Hydrosilylation. *Nat Commun* 2018, 9 (1), 221. https://doi.org/10.1038/s41467-017-02472-6.

- (59) Slater, J. W.; Marguet, S. C.; Gray, M. E.; Monaco, H. A.; Sotomayor, M.; Shafaat, H. S. Power of the Secondary Sphere: Modulating Hydrogenase Activity in Nickel-Substituted Rubredoxin. ACS Catal. 2019, 9 (10), 8928–8942.
 https://doi.org/10.1021/acscatal.9b01720.
- (60) Wertz, A. E.; Teptarakulkarn, P.; Stein, R. E.; Moore, P. J.; Shafaat, H. S. Rubredoxin Protein Scaffolds Sourced from Diverse Environmental Niches as an Artificial Hydrogenase Platform. *Biochemistry* 2023, 62 (17), 2622–2631. https://doi.org/10.1021/acs.biochem.3c00249.
- (61) Slater, J. W.; Marguet, S. C.; Cirino, S. L.; Maugeri, P. T.; Shafaat, H. S. Experimental and DFT Investigations Reveal the Influence of the Outer Coordination Sphere on the Vibrational Spectra of Nickel-Substituted Rubredoxin, a Model Hydrogenase Enzyme. *Inorg. Chem.* 2017, 56 (7), 3926–3938. https://doi.org/10.1021/acs.inorgchem.6b02934.

Table of Contents Graphic



Directly coupling catalysts to light absorbers represents a promising strategy for solar fuel formation, but how to optimally match each component is not well understood. In this work, a series of phototriggers were bound to an artificial metalloenzyme for light-driven hydrogen production and characterized using time-resolved spectroscopy and activity assays. As hypothesized, the H₂ generated correlates with excited-state reduction potentials, though competing photophysical factors were found to have a significant impact on overall activity.